https://doi.org/10.1038/s41586-018-0221-0

Self-assembly of highly symmetrical, ultrasmall inorganic cages directed by surfactant micelles

Kai Ma[1], Yunye Gong[2], Tangi Aubert[1,3], Melik Z. Turker[1], Teresa Kao[1], Peter C. Doerschuk[2,4] & Ulrich Wiesner[1]*

Nanometre-sized objects with highly symmetrical, cage-like polyhedral shapes, often with icosahedral symmetry, have recently been assembled from DNA[1–3], RNA[4] or proteins[5,6] for applications in biology and medicine. These achievements relied on advances in the development of programmable self-assembling biological materials[7–10], and on rapidly developing techniques for generating three-dimensional (3D) reconstructions from cryo-electron microscopy images of single particles, which provide high-resolution structural characterization of biological complexes[11–13]. Such single-particle 3D reconstruction approaches have not yet been successfully applied to the identification of synthetic inorganic nanomaterials with highly symmetrical cage-like shapes. Here, however, using a combination of cryo-electron microscopy and single-particle 3D reconstruction, we suggest the existence of isolated ultrasmall (less than 10 nm) silica cages ('silicages') with dodecahedral structure. We propose that such highly symmetrical, self-assembled cages form through the arrangement of primary silica clusters in aqueous solutions on the surface of oppositely charged surfactant micelles. This discovery paves the way for nanoscale cages made from silica and other inorganic materials to be used as building blocks for a wide range of advanced functional-materials applications.

In our search for dodecahedral silica-cage structures (Fig. 1), we began with the early stages in the self-assembly of silica structures directed by surfactant micelles[14]. Our synthesis system contained cetyltrimethylammonium bromide (CTAB) surfactant micelles and tetramethyl orthosilicate (TMOS) as a sol–gel silica precursor (see Methods). We added hydrophobic mesitylene (TMB) into the aqueous CTAB micelle solution, increasing the size and deformability of the micelles[15]. We selected TMOS as the silica source because of its fast hydrolysis rate in water, and we adjusted the initial reaction pH to about 8.5. When TMOS was added, its hydrolysis to silicic acid reduced the reaction pH to neutral[16,17]. The lowered pH accelerated silane condensation, leading to primary silica clusters[18] with diameters of around 2 nm. The negatively charged silica clusters were attracted to the positively charged CTAB micelle surface, assembling into micelle-templated nanostructures[14]. This experimental design—in which fast hydrolysis and condensation of the silica precursor quickly terminated the reaction—allowed the early stages in the micelle-directed self-assembly of silica structures to be preserved[17].

In order to improve the dispersity of particles on transmission electron microscopy (TEM) grids, we added low-molar-mass, silane-modified monofunctional polyethylene glycol (PEG) into the solution one day before preparing TEM samples. This process covalently coated the accessible silica surface[19], yielding PEGylated nanoparticles (Extended Data Fig. 1) that could be further purified and isolated from the synthesis solution. Using TEM, we observed particles of narrow size distribution, with an average diameter of around 12 nm (Fig. 2a, including inset), consistent with silica structures wrapped around TMB-swollen CTAB micelles[15]. The detailed particle structure was difficult to identify, however. Therefore, we plasma-etched TEM samples on carbon grids for five seconds before imaging in order to remove excess organic chemicals (such as PEG-silane) that would otherwise contribute to background noise. To further improve the signal-to-noise ratio, we acquired and averaged a series of images of the same sample area. Stripes and windows in zoomed-in images of individual particles became more clearly recognizable, suggesting the presence of cage-like structures (Fig. 2b, including insets).

Analysis of thousands of such single-particle TEM images revealed the prevalence of two cage projections, one with two-fold symmetry and one with five-fold symmetry (Fig. 2c)—too few to allow a successful 3D reconstruction. We therefore shifted our attention to cryo-electron microscopy (cryo-EM) characterization of the native reaction solution. We omitted the silica-surface PEGylation step, as the high PEG concentration substantially increased the sensitivity of the samples to radiation, resulting in difficulties in obtaining clear cryo-EM images.

Cryo-EM provided direct visualization of particles in solution with arbitrary orientation—that is, without disturbances resulting from drying of the samples on TEM substrates, including structure deflation. The background noise was much reduced because of the absence of a TEM substrate and of chemicals dried onto the substrate during sample preparation (Fig. 2c). Although particle aggregation was observed occasionally through cryo-EM (Fig. 2d), individual silica nanoparticles with cage-like structures could always be identified (Fig. 2c, d). No particle aggregation was observed in dry-state TEM of PEGylated particles, suggesting that particle aggregation observed by cryo-EM was a reversible process that could be overcome via insertion of PEG chains.

We manually identified around 19,000 single-particle images from cryo-EM micrographs, then clustered them and averaged the images in each cluster in order to improve the signal-to-noise ratio[20]. The averages showed different orientations of silica nanoparticles with cage-like structures (silicages; Extended Data Fig. 2a). We identified averages that were consistent with selected projections of a pentagonal dodecahedral cage (Fig. 2c and Extended Data Fig. 2b). The dodecahedral silicage (icosahedral point group, I_h; Fig. 1) is the simplest of a set of Voronoi polyhedra suggested to form the smallest structural

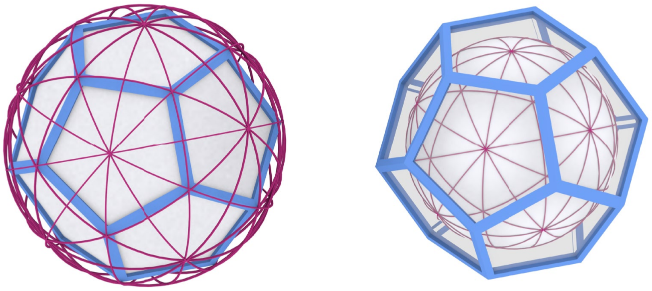

Fig. 1 | Representations of a dodecahedron. Left, among the platonic solids, the dodecahedron best fills out its circumscribed sphere—that is, a sphere that passes through all of its vertices. Right, the inscribed sphere that passes through all of the dodecahedron's facets is shown for comparison.

---

[1]Department of Materials Science and Engineering, Cornell University, Ithaca, NY, USA. [2]School of Electrical and Computer Engineering, Cornell University, Ithaca, NY, USA. [3]Department of Chemistry, Ghent University, Ghent, Belgium. [4]Nancy E. and Peter C. Meinig School of Biomedical Engineering, Cornell University, Ithaca, NY, USA. *e-mail: ubw1@cornell.edu

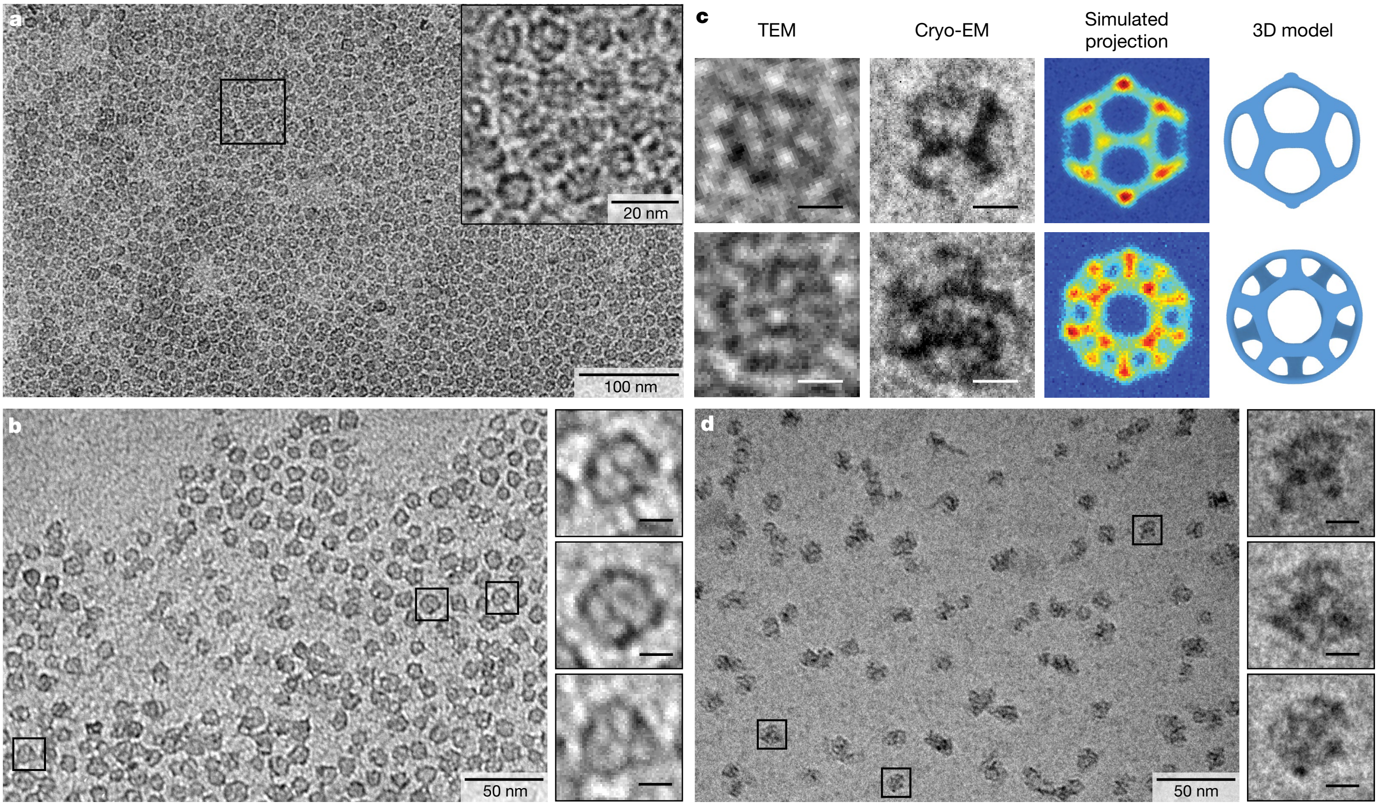

Fig. 2 | TEM and cryo-EM characterizations of silicages. a, Low-magnification TEM images of PEG-coated silicages on a carbon substrate. The inset is a zoomed-in image. **b**, Averaged TEM image obtained using 11 images of the same sample area of PEG-coated silicages; insets show representative individual structures at a higher magnification. The sample was plasma etched for five seconds before TEM characterization to reduce background noise. **c**, Comparison of silicages observed by TEM and cryo-EM with projections of simulated dodecahedral cages and models. **d**, Cryo-EM images of silicages without PEG coating. Scale bars in the insets of **b**–**d** represent 5 nm.

units of multiple forms of mesoporous silica[21]. Although such highly symmetrical ultrasmall silica cages have, to our knowledge, never been isolated before, it had seemed likely that this should be possible.

Guided by this structural insight, we carried out single-particle 3D reconstructions of silicages using the ‘Hetero’[22] model-based maximum likelihood machine-learning algorithm, in which a two-class reconstruction is computed to overcome challenges associated with structural heterogeneity (see Methods) and rotational icosahedral symmetry is imposed on both classes (Extended Data Fig. 2). One of the two-class reconstructions was a dodecahedral cage, as visualized by UCSF Chimera (ref. [23]; Fig. 3a, b). We identified a low-intensity signal inside this reconstructed cage, consistent with the presence of TMB-swollen CTAB micelles within the silicage, whose electron density is lower than that of silica but higher than that of the surrounding ice. The other class of reconstruction did not provide an interpretable structure, probably owing to heterogeneity in the structure of the corresponding particles. We carried out such two-class reconstructions using different numbers of single-particle images (2,000, 7,000 and 10,000) and found consistent results. We further performed single-class reconstructions with the Hetero algorithm, using only images from the class that showed dodecahedral cages in two-class reconstructions. Equivalent two-class and single-class reconstructions were also performed with the widely used RELION 2.1 system[24,25]. Dodecahedral cage structures were obtained in all of these reconstructions (Extended Data Fig. 3 and Supplementary Videos 1, 2). The resolution of the reconstructions was approximately 2 nm (ref. [26]; Extended Data Fig. 4). Silica in these cages is amorphous at the atomic level, which prevented atomic resolution of these reconstructions.

The Hetero reconstruction algorithm provided estimates of the projected orientation (that is, three Euler angles) for each experimental image, which we used to compute predicted projections. Nine predicted projections and corresponding experimental images were manually clustered, and averages were computed for each cluster (Fig. 3c). The similarity of the projections of the 3D reconstruction and the averaged experimental images supports the dodecahedral cage structure. Furthermore, we calculated the theoretical probabilities of finding each of the nine projections (Fig. 3c) on the basis of the assumption that the orientations of silicages in cryo-EM are random. We then compared the results with the probabilities observed by single-particle 3D reconstruction (Extended Data Fig. 5). The high consistency between the theoretical and experimental projection probabilities further supports the dodecahedral cage reconstruction.

At this early point we can only speculate about the exact mechanism by which the observed silicage structure is formed, but there are clues in the details of the reconstruction. The silica occupying the vertices of the dodecahedral cage has a diameter of around 2.4 nm (Fig. 3b)—only slightly larger than the diameter of primary silica clusters, being approximately 2 nm (ref. [18]; Extended Data Fig. 6). The interstitial spacing between two nearby vertices is estimated to be about 1.4 nm (this is the length of an edge, 3.8 nm, minus the diameter of the vertices, 2.4 nm; see Fig. 3b), which is much less than the diameter of such clusters. Bridges between vertices forming the edges of the dodecahedron are substantially thinner than the size of the primary clusters (Fig. 3a, b). This suggests that negatively charged primary silica clusters formed in solution may start to descend onto the positively charged micelle surface, attracted by Coulomb interactions. As more and more silica clusters assemble on the micelle surface, their repulsive interactions and possible interactions with other micelles may cause them to move to the vertices of a dodecahedron. Further silane condensation onto the surface of growing clusters may lead eventually to bridge formation, resulting in the final observed cage structure (Fig. 3). The origin of icosahedral symmetry in viruses has been associated with the energy minimization

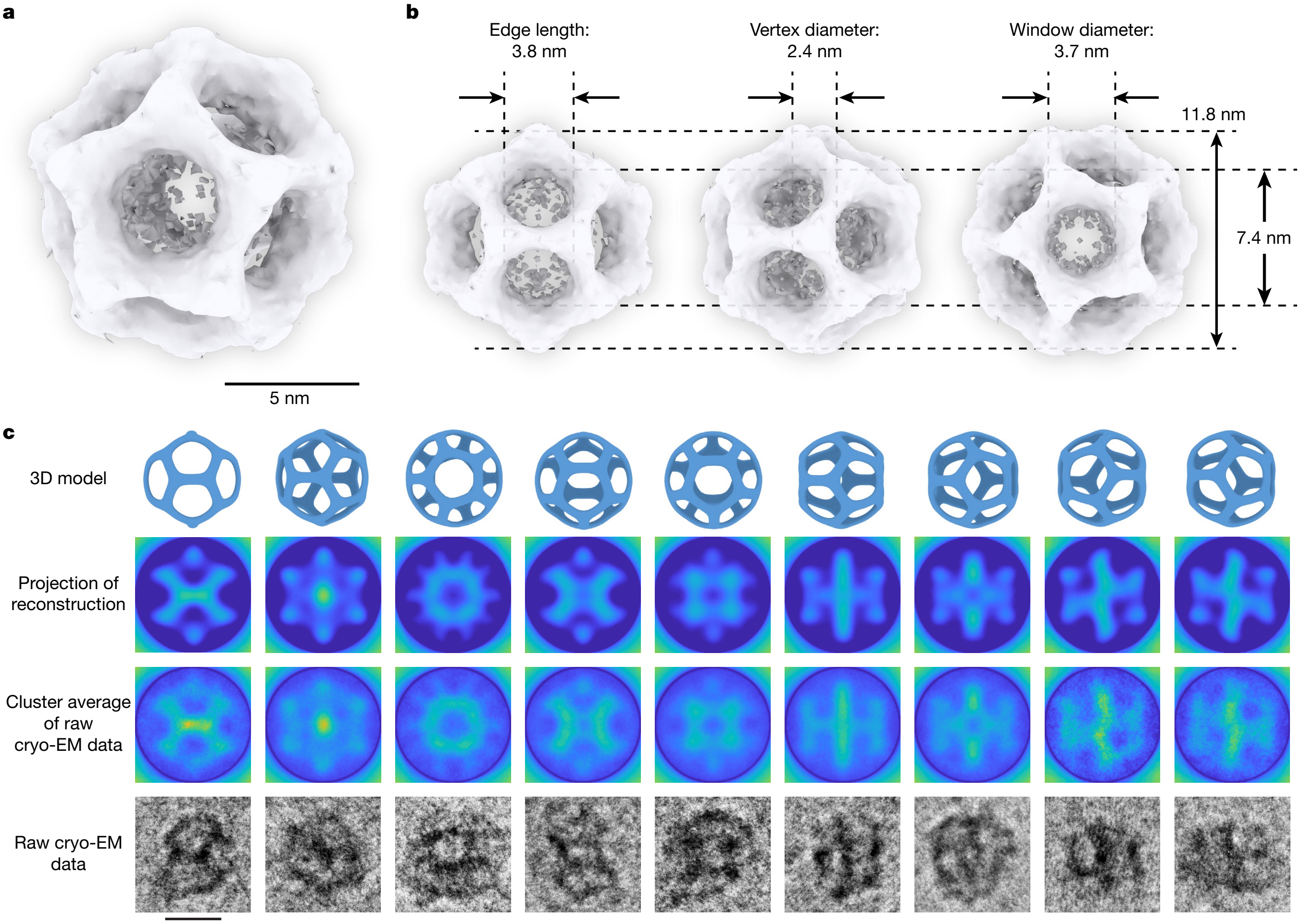

Fig. 3 | Single-particle reconstruction of the dodecahedral silicage. **a**, **b**, Reconstruction of the dodecahedral silicage (**a**), and its three most unique projections along the two-fold, three-fold and five-fold symmetry axes (**b**). The average dimensions of silicages in **b** were estimated from the reconstructed dodecahedral silicage. **c**, Representative comparison of nine unique projections from the reconstruction and cryo-EM cluster averages with projections of a 3D dodecahedral cage model. Corresponding single cryo-EM images are shown at the bottom, highlighting the difference between the raw data and the reconstruction. The scale bar in **c** represents 10 nm. The visualizations in **a** and **b** were made using UCSF Chimera[23].

of two opposing interactions: repulsive interactions associated with bending rigidity, and attractive hydrophobic interactions[27]. In a similar way, in addition to electrostatic interactions, deformation of the micelle surface around the silica clusters may be another important contributor to the free energy in our system. This idea is supported by experiments showing that the cage structures do not form in the absence of TMB (Extended Data Fig. 7), which is expected to enhance the deformability of the micelle surface.

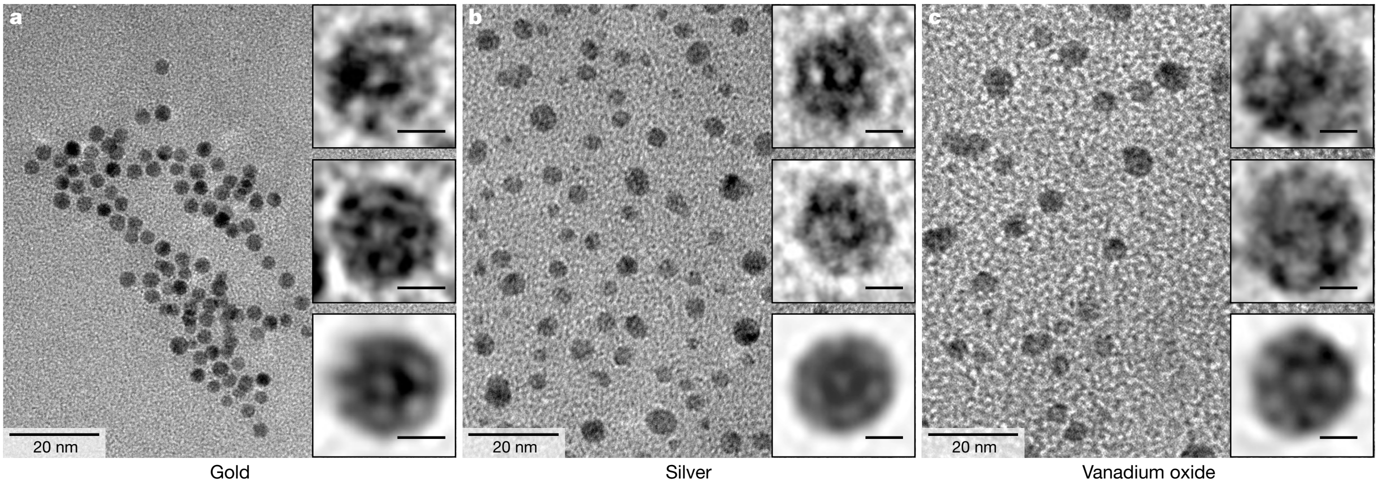

Fig. 4 | Cage-like structures with different inorganic compositions. **a**–**c**, Cage-like nanoparticles similar to silicages were obtained when silica was replaced by other materials, including gold (**a**), silver (**b**) or vanadium oxide (**c**). The insets show zoomed-in images of individual particles (top two rows) and averaged images[20] (bottom row). The scale bars in all insets represent 2 nm.

We have found that the self-assembly of ultrasmall cage structures directed by surfactant micelles can also occur when using other inorganic materials that have similarly sized features and similar surface chemistry to silica. In preliminary experiments, we replaced silica with one of two metals, gold or silver, or a transition metal oxide, vanadium oxide. Gold and silver structures were prepared by the reduction of metal precursors—gold chloride trihydrate and silver nitrate, respectively—in the presence of the micelles (Extended Data Fig. 8; see Methods). We used tetrakis(hydroxymethyl)phosphonium chloride (THPC) as both the reductant and the capping agent to stabilize primary gold and silver nanoparticles and to provide negative surface charges[28]. By contrast, primary vanadium oxide nanoparticles with a native negatively charged particle surface were prepared via sol–gel chemistry[29], in a similar way to the synthesis of silicages (see Methods). Images of individual particles obtained by TEM revealed similar internal structures (Fig. 4). These nanoparticles did not appear to be dense but instead showed cage-like structures (compare Figs. 2 and 4), as corroborated by associated projection averages[20] revealing cages with rotational symmetry (bottom insets in Fig. 4), similar to the prevalent projection in case of the silicage (vide supra). Therefore, micelle-self-assembly-directed cages like the dodecagonal structures described here may not be unique to amorphous silica, but may provide direct synthesis pathways to crystalline material cages (Extended Data Fig. 9).

There are several ramifications of our silicage discovery. First, such cages are generally considered to be individual structural units from which larger-scale mesoporous silica is built in a bottom-up manner[15,21]. However, given that a dodecahedron cannot be used to generate a tessellation of 3D space, other silica cage structures must be required. This knowledge should motivate better understanding of the early formation pathways of surfactant-directed silica self-assembly, including a search for micelle-directed ultrasmall silicages with other structures, and from other materials (vide supra). Second, the chemical and practical value of this polyhedral structure may prove immense. Given the versatility of silica surface chemistry, and the ability to distinguish the inside and outside of the cage via micelle-directed synthesis[17], one can readily conceive of cage derivatives of many kinds, which may exhibit unusual properties and be useful in applications ranging from catalysis to drug delivery. For example, given recent success in the clinical translation of ultrasmall fluorescent silica nanoparticles with similar particle sizes and surface properties to those described here[30], one can envisage a range of new diagnostic and therapeutic probes with drugs hidden inside the cages.

Online content

Any Methods, including any statements of data availability and Nature Research reporting summaries, along with any additional references and Source Data files, are available in the online version of the paper at https://doi.org/10.1038/s41586-018-0221-0

Received: 17 December 2017; Accepted: 20 April 2018;
Published online 20 June 2018.

1. He, Y. et al. Hierarchical self-assembly of DNA into symmetric supramolecular polyhedra. *Nature* **452**, 198–201 (2008).
2. Douglas, S. M. et al. Self-assembly of DNA into nanoscale three-dimensional shapes. *Nature* **459**, 414–418 (2009); erratum **459**, 1154 (2009).
3. Iinuma, R. et al. Polyhedra self-assembled from DNA tripods and characterized with 3D DNA-PAINT. *Science* **344**, 65–69 (2014).
4. Afonin, K. A. et al. *In vitro* assembly of cubic RNA-based scaffolds designed in silico. *Nat. Nanotechnol.* **5**, 676–682 (2010).
5. King, N. P. et al. Computational design of self-assembling protein nanomaterials with atomic level accuracy. *Science* **336**, 1171–1174 (2012).
6. Hsia, Y. et al. Design of a hyperstable 60-subunit protein icosahedron. *Nature* **535**, 136–139 (2016); corrigendum **540**, 150 (2016).
7. Rothemund, P. W. Folding DNA to create nanoscale shapes and patterns. *Nature* **440**, 297–302 (2006).
8. Yin, P., Choi, H. M. T., Calvert, C. R. & Pierce, N. A. Programming biomolecular self-assembly pathways. *Nature* **451**, 318–322 (2008).
9. Ke, Y., Ong, L., Shih, W. & Yin, P. Three-dimensional structures self-assembled from DNA bricks. *Science* **338**, 1177–1183 (2012).
10. King, N. P. et al. Accurate design of co-assembling multi-component protein nanomaterials. *Nature* **510**, 103–108 (2014).
11. Zhao, M. et al. Mechanistic insights into the recycling machine of the SNARE complex. *Nature* **518**, 61–67 (2015).
12. Fernandez-Leiro, R. & Scheres, S. H. W. Unravelling biological macromolecules with cryo-electron microscopy. *Nature* **537**, 339–346 (2016).
13. Dai, X. et al. In situ structures of the genome and genome-delivery apparatus in a single-stranded RNA virus. *Nature* **541**, 112–116 (2017).
14. Kresge, C. T., Leonowicz, M. E., Roth, W. J., Vartuli, J. C. & Beck, J. S. Ordered mesoporous molecular sieves synthesized by a liquid-crystal template mechanism. *Nature* **359**, 710–712 (1992).
15. Sun, Y. et al. Formation pathways of mesoporous silica nanoparticles with dodecagonal tiling. *Nat. Commun.* **8**, 252 (2017).
16. Ma, K. et al. Control of ultrasmall sub-10 nm ligand-functionalized fluorescent core–shell silica nanoparticle growth in water. *Chem. Mater.* **27**, 4119–4133 (2015).
17. Ma, K., Sai, H. & Wiesner, U. Ultrasmall sub-10 nm near-infrared fluorescent mesoporous silica nanoparticles. *J. Am. Chem. Soc.* **134**, 13180–13183 (2012).
18. Carcouët, C. C. M. C. et al. Nucleation and growth of monodisperse silica nanoparticles. *Nano Lett.* **14**, 1433–1438 (2014).
19. Ma, K., Zhang, D., Cong, Y. & Wiesner, U. Elucidating the mechanism of silica nanoparticle PEGylation processes using fluorescence correlation spectroscopies. *Chem. Mater.* **28**, 1537–1545 (2016).
20. Tang, G. et al. EMAN2: an extensible image processing suite for electron microscopy. *J. Struct. Biol.* **157**, 38–46 (2007).
21. Xiao, C., Fujita, N., Miyasaka, K., Sakamoto, Y. & Terasaki, O. Dodecagonal tiling in mesoporous silica. *Nature* **487**, 349–353 (2012).
22. Gong, Y., Veesler, D., Doerschuk, P. C. & Johnson, J. E. Effect of the viral protease on the dynamics of bacteriophage HK97 maturation intermediates characterized by variance analysis of cryo EM particle ensembles. *J. Struct. Biol.* **193**, 188–195 (2016).
23. Pettersen, E. F. et al. UCSF Chimera—a visualization system for exploratory research and analysis. *J. Comput. Chem.* **25**, 1605–1612 (2004).
24. Scheres, S. H. W. RELION: implementation of a Bayesian approach to cryo-EM structure determination. *J. Struct. Biol.* **180**, 519–530 (2012).
25. Rohou, A. & Grigorieff, N. CTFFIND4: fast and accurate defocus estimation from election micrographs. *J. Struct. Biol.* **192**, 216–221 (2015).
26. Harauz, G. & van Heel, M. Exact filters for general geometry three dimensional reconstruction. *Optik* **73**, 146–156 (1986).
27. Zandi, R., Reguera, D., Bruinsma, R. F., Gelbart, W. M. & Rudnick, J. Origin of icosahedral symmetry in viruses. *Proc. Natl Acad. Sci. USA* **101**, 15556–15560 (2004).
28. Duff, D. G., Baiker, A. & Edwards, P. P. New hydrosol of gold clusters. 1. Formation and particle size variation. *Langmuir* **9**, 2301–2309 (1993).
29. Sullivan, L. M., Li, L. & Lukehart, C. M. Synthesis of VO_2 nanopowders. Part I. Sol–gel processing of vanadium alkoxide precursor within inverse micelles. *J. Cluster Sci.* **25**, 313–322 (2014).
30. Phillips, E. et al. Clinical translation of an ultrasmall inorganic optical-PET imaging nanoparticle probe. *Sci. Transl. Med.* **6**, 260ra149 (2014).

Acknowledgements This project was supported by the National Cancer Institute of the National Institutes of Health under award number U54CA199081. Y.G. and P.C.D. acknowledge financial support from the National Science Foundation (NSF) under grant number 1217867, and Y.G. acknowledges financial support from a 2017 Google PhD Fellowship in Machine Learning. T.A. acknowledges financial support from the Ghent University Special Research Fund (BOF14/PDO/007) and the European Union's Horizon 2020 research and innovation program (MSCA-IF-2015-702300 and MSCA-RISE-691185). M.Z.T. acknowledges fellowship support from the Ministry of National Education of the Republic of Turkey. This work used shared facilities of the Cornell Center for Materials Research, with funding from the NSF Materials Research Science and Engineering Center program (DMR-1719875), as well as the Nanobiotechnology Center's shared research facilities at Cornell. The authors thank V. Elser, Y. Jiang and D. Zhang for helpful discussions.

Author contributions K.M., T.A. and U.W. designed the experimental work. Y.G. and P.C.D. performed the reconstructions. K.M. synthesized the silica-based materials. T.A. synthesized the metal-based and transition-metal-oxide-based materials. K.M. and T.A. performed TEM and cryo-EM characterization. K.M., T.A., M.Z.T. and T.K. processed the images for reconstructions. K.M., T.A. and U.W. discussed the experimental work. U.W. wrote the manuscript with input from all co-authors. U.W. supervised the work.

Competing interests The authors declare that they have submitted a patent disclosure based on this study through Cornell University.

Additional information
Extended data is available for this paper at https://doi.org/10.1038/s41586-018-0221-0.
Supplementary information is available for this paper at https://doi.org/10.1038/s41586-018-0221-0.
Reprints and permissions information is available at http://www.nature.com/reprints.
Correspondence and requests for materials should be addressed to U.W.
Publisher's note: Springer Nature remains neutral with regard to jurisdictional claims in published maps and institutional affiliations.

METHODS

Chemicals and materials. All chemicals were used as received. Cetyltrimethylammonium bromide (CTAB), ammonia (2 M in ethanol), mesitylene (1,3,5 trimethylbenzene; TMB), tetramethyl orthosilicate (TMOS), gold chloride trihydrate ($HAuCl_4{\cdot}3H_2O$), silver nitrate ($AgNO_3$), tetrakis(hydroxymethyl) phosphonium chloride (THPC), dimethyl sulfoxide (DMSO), acetic acid and ethanol were purchased from Sigma-Aldrich. Vanadium oxytriisopropoxide was purchased from Alfa Aesar. Anhydrous potassium carbonate (K_2CO_3) was purchased from Mallinckrodt. Anhydrous ethanol was purchased from Koptec. Silane-modified monofunctional polyethylene glycol (PEG-silane) with a molar mass of around 500 g mol^{-1} (six to nine ethylene glycol units) was purchased from Gelest. Carbon-film-coated copper grids for TEM, and C-Flat holey carbon grids for cryo-EM, were purchased from Electron Microscopy Sciences.

Synthesis, TEM and cryo-EM characterization of silicages. Silicages were synthesized in aqueous solution through surfactant-directed silica condensation. 125 mg of CTAB was first dissolved in 10 ml of ammonium hydroxide solution (0.002 M). Then, 100 μl TMB was added to expand the CTAB micelle size; the water/CTAB/TMB molar ratio was about 1,620/1/2. The solution was stirred at 600 r.p.m. at 30 °C overnight, and then 100 μl TMOS was added. The reaction was then left again at 30 °C overnight under stirring at 600 r.p.m.

To prepare cryo-EM samples, we applied 5 μl of the native reaction solution to a glow-discharged CF-4/2-2C Protochips C-Flat holey carbon grid, which was then blotted using filter paper and plunged into a liquid mixture of 37% ethane and 63% propane at −194 °C using an Electron Microscopy Science plunge freezer. Cryo-EM images were acquired on a FEI Tecnai F20-ST TEM operated at an acceleration voltage of 200 kV using a Gatan Orius charge-coupled-device (CCD) camera. All cryo-EM images used for reconstruction were acquired at the same magnification, with a pixel size of 0.16 nm, and nominal defocus was kept between 1 μm and 2 μm.

To prepare dry-state TEM samples, we added 100 μl of PEG-silane into the reaction solution. The reaction solution was left at 30 °C overnight under stirring at 600 r.p.m. to surface-modify silicages covalently with PEGs, in order to improve their dispersity on TEM grids. Afterwards, 30 μl of the reaction solution was dropped onto a copper grid coated with a continuous carbon film, and blotted using filter paper. TEM images were acquired using a FEI Tecnai T12 Spirit microscope operated at an acceleration voltage of 120 kV. In order to improve the signal-to-noise ratio in recorded images, TEM sample grids were plasma etched for 5 seconds before TEM characterization, and a series of images was acquired of the same sample area, which were then averaged.

In order to quench individual primary silica clusters formed at the very early stages of cage formation, we added 100 μl of PEG-silane into the reaction solution about three minutes after the addition of TMOS. The remainder of the procedures—including particle synthesis, dry-state TEM sample preparation, and TEM characterization—were as described above.

Particle purification. In order to remove CTAB and TMB from the cages, after adding PEG-silane and stirring at 30 °C for a day (see above), we heat-treated the solution at 80 °C overnight to further enhance the covalent attachment of PEG-silane to the silica surface of the silicages. The PEGylated nanocages were dialysed (with a molecular weight cut-off, MWCO, of 10 kDa) in a mixture of acetic acid, ethanol and water (volume ratio 7/500/500) for three days, and then in deionized water for another three days[17]. In both cases the dialysis solutions were changed once per day. The dry-state TEM sample preparation and TEM characterization methods were as described above.

Synthesis of particles without TMB. The synthesis and TEM characterization methods used for particles without TMB were the same as those for particles with TMB, as described above, except that the TMB addition step was omitted.

Silicage surface area and yield of production. We assessed the specific surface area of the silicages through a combination of nitrogen sorption measurements and theoretical estimations. After the synthesis and purification of PEGylated silicages, particles were first upconcentrated using a spin filter (Vivaspin 20, MWCO 10 kDa) and dried at 60 °C. Particles were then calcined at 550 °C for 6 hours in air. The production yield was then estimated by dividing the remaining weight after calcination, that is, the weight of inorganic silica, by the theoretical weight of silica, that is, the weight calculated on the basis of the amount of silica source added into the synthesis. Nitrogen adsorption and desorption isotherms were acquired using a Micromeritics ASAP 2020 (Extended Data Fig. 1c), yielding a specific surface area of 570 m^2 g^{-1} by the Brunauer−Emmett−Teller (BET) method. For comparison, using the dodecahedral cage model with the dimensions from the reconstruction shown in Fig. 3, we estimated the theoretical surface area of silicages to be around 790 m^2 g^{-1}. The lower experimental value is consistent with the expected losses of surface area during sample calcination.

Synthesis and TEM of metal cage-like structures. The gold and silver cage-like structures were prepared by the reduction of metal precursors—$HAuCl_4{\cdot}3H_2O$ and $AgNO_3$, respectively—in the presence of micelles with the same water/CTAB/TMB ratio as for the silicage work. In a typical batch, 50 mg of CTAB was dissolved in 4 ml of water at 30 °C, then 40 μl of TMB and 200 μl of ethanol were added to the mixture. After stirring the reaction at 30 °C overnight at 600 r.p.m., 16 μl of either $HAuCl_4{\cdot}3H_2O$ (25 mM) or $AgNO_3$ (25 mM) was added, followed after 5 min by 8 μl of THPC (68 mM). After another 5 min, 6 μl of potassium carbonate (0.2 M) was added.

Dry-state TEM samples of gold and silver cage-like structures were prepared after one day and 6 hours of reaction, respectively, owing to the different reaction rates as described in further synthesis Methods sections below. In both cases, the samples were prepared by drying 8 μl of the native reaction mixture diluted three times in ethanol on a TEM grid in air overnight. In order to remove the thick CTAB layer before imaging, the grid was immersed in ethanol for 2 min and then dried in air. TEM images of metal cage-like structures were acquired using a FEI Tecnai T12 Spirit microscope operated at an acceleration voltage of 120 kV.

Synthesis and TEM of metal oxide structures. Vanadium oxide cage-like structures were prepared on the basis of sol–gel chemistry in a similar way to the silicages, using vanadium oxytriisopropoxide as the precursor. In a typical batch, 50 mg of CTAB was dissolved in 4 ml of water at 30 °C, and then 40 μl of TMB were added. After stirring the reaction at 30 °C overnight at 600 r.p.m., 50 μl of vanadium oxytriisopropoxide diluted in 100 μl of DMSO were added.

Dry-state TEM samples for vanadium oxide cage-like structures were prepared after one day of reaction by drying on a TEM grid 8 μl of the native reaction mixture, diluted ten times in water. At such a dilution, the amount of CTAB was low enough that the TEM samples did not require any plasma cleaning or soaking in ethanol before imaging. The TEM images of vanadium oxide cages were acquired using a FEI Tecnai T12 Spirit microscope operated at an acceleration voltage of 120 kV.

Particle reconstruction. We used the 'Hetero' model-based maximum likelihood machine-learning algorithm[22] for particle reconstruction. This algorithm can simultaneously estimate: (1) a reconstruction for each type of particle shown in the images; (2) the type of particle shown in each image; and (3) the projection orientation for each image. Such a joint estimation is a central feature of the algorithm and is a natural approach for processing data from complicated mixtures. The estimates in (2) and (3), which are based on 3D structure, are independent of the clustering of 2D images, which is based on pixel values (see, for example, Extended Data Fig. 2). In addition to the Hetero algorithm, we applied the widely used RELION 2.1 system[24] to compute equivalent two-class and single-class reconstructions. The images were corrected for the contrast transfer function (CTF) by phase flipping.

Further details of metal- and metal-oxide-based cages. In contrast to the sol–gel reaction that produces the silicage, synthesis of the gold and silver cage-like structures relies on reduction reactions. To this end, we used THPC because it reacts in water at basic pH to form trimethoxyphosphine, which can be both the reductant and the capping agent for the metal nanoparticles. THPC has been widely used to synthesize ultrasmall (less than 3 nm) and negatively charged phosphine-stabilized gold nanoparticles[28]. These nanoparticles are often used as seeds for the subsequent growth of continuous gold shells on the surface of aminated silica nanoparticles thanks to their high affinity and binding efficiency with amine groups[31,32]. Alcohol was added to the reaction mixture in order to mimic the conditions of the silicage synthesis, where methanol is formed upon hydrolysis of TMOS. Early-stage preliminary experiments showed that the resulting metal structures improved in size dispersity when using ethanol at a slightly higher concentration than that of the released methanol in the silicage synthesis. Gold and silver cage-like structure syntheses were performed at a much lower concentration (silver or gold concentration = 93.7 μM) than that of the silicages (silica precursor concentration = 65.9 mM). Attempts at synthesizing gold and silver cages at higher concentrations resulted in much larger nanoparticles with no apparent internal structure.

Gold-based synthesis. The addition of gold precursor to the reaction initially resulted in the formation of a pale yellow precipitate that turned into a clear (that is, non-turbid), darker-orange solution within a couple of minutes under stirring at 30 °C (see Extended Data Fig. 8 for a survey of the absorption characteristics at each step of the synthesis). Given that neither the precipitate nor the darker-orange colouration was observed in the absence of CTAB, we attribute these observations to some interaction between the gold chloride anions and the ammonium groups of the CTAB. After the addition of THPC, the solution turned colourless within a couple of minutes, indicating that gold(III) had been reduced to gold(I). The subsequent transformation of THPC into trimethoxyphosphine, following an increase in pH through the addition of potassium carbonate, happened within the first hour of reaction (see also the description of silver-based synthesis below). However, the reduction from gold(I) to gold(0) was rather slow, with the first hint of colouration appearing after 8 hours of reaction. After one day of reaction, the solution exhibited a brown colouration. This colouration is the signature of gold nanoparticles that are too small or not dense enough to exhibit a strong surface plasmon resonance, as shown by the absorption profile in Extended Data Fig. 8, which shows only a faint feature around 510 nm.

Silver-based synthesis. The addition of silver precursor to the reaction did not initially translate into any visible effects, either in the presence of CTAB/TMB or after adding THPC. Nevertheless, after adding potassium carbonate to the silver-based synthesis, the solution started to turn pale yellow within the first hour of reaction and resulted in an intense yellow colouration after 6 hours, at which point we prepared the TEM samples. This yellow colouration is typical of small silver nanoparticles with a surface plasmon resonance centred around 420 nm (Extended Data Fig. 8).

Vanadium-oxide-based synthesis. The vanadium oxide cage-like nanoparticles were prepared under the same conditions as the silicages; however, the pH was not adjusted with ammonia owing to the fast hydrolysis and condensation rate of the vanadium oxide precursor. Unlike in the synthesis of metal cage-like nanoparticles, no alcohol was added here, because the hydrolysis of the vanadium precursor—vanadium oxytriisopropoxide—produces alcohol at concentrations similar to those used in the silicage synthesis. The addition of this precursor to the TMB micelles resulted in the immediate formation of a red precipitate. Under stirring, the precipitate dispersed homogeneously in solution, which remained turbid, and turned orange after one day of reaction at 30 °C.

Data availability. Figures that have associated raw data are Figs. 2–4 and Extended Data Figs. 1–4, 5c and 6–9. There are no restrictions on data availability. The data sets generated and analysed during this study are available from the corresponding author on reasonable request.

Code availability. The custom code and algorithm used for the 3D reconstruction and related analysis are available from the corresponding author on reasonable request.

31. Westcott, S. L., Oldenburg, S. J., Lee, T. R. & Halas, N. J. Formation and adsorption of clusters of gold nanoparticles onto functionalized silica nanoparticle surfaces. *Langmuir* **14**, 5396–5401 (1998).
32. Ji, B. et al. Non-blinking quantum dot with a plasmonic nanoshell resonator. *Nat. Nanotechnol.* **10**, 170–175 (2015).

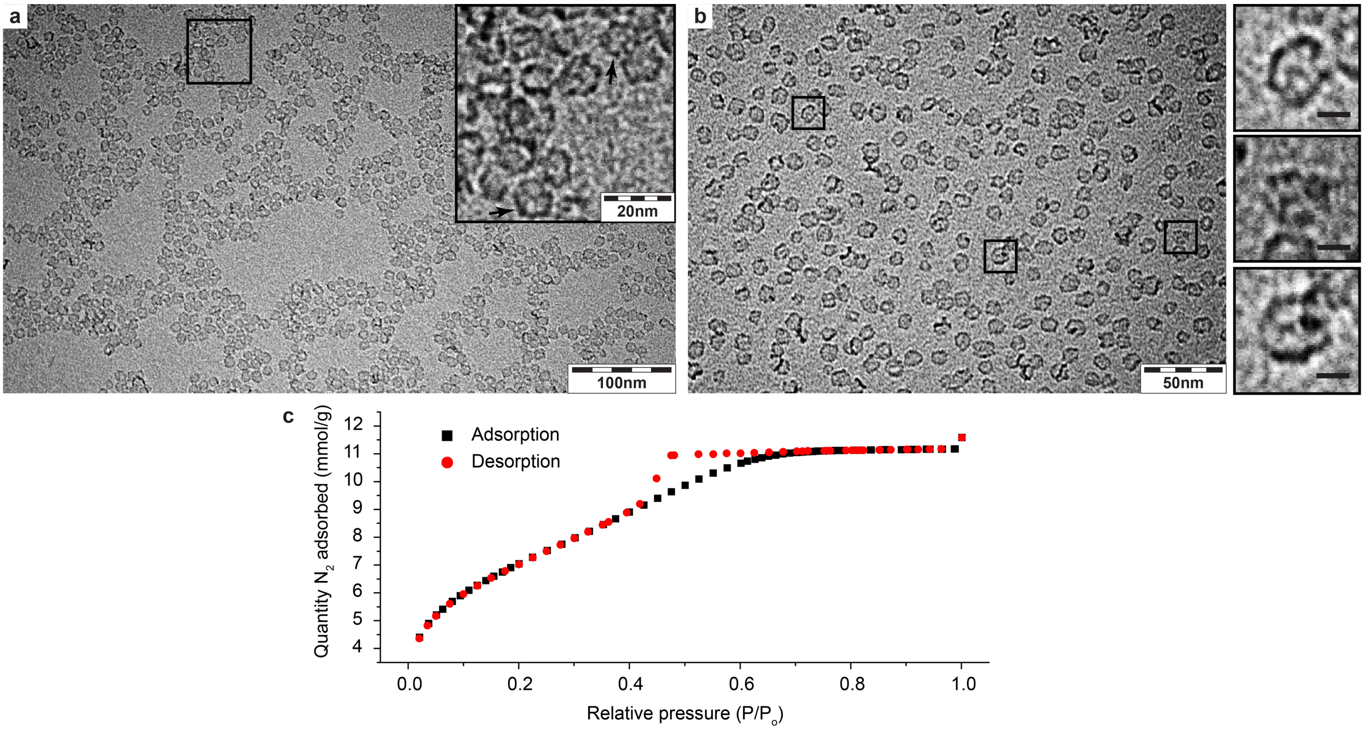

Extended Data Fig. 1 | PEGylated silicages after cleaning, and nitrogen sorption measurements on calcined cages. a, **b**, Representative dry-state TEM images, at different magnifications, of PEGylated silicages after the removal of surfactant (CTAB) and TMB (see Methods). The insets in **a** (black arrows) and **b** reveal cage-like structures, suggesting structure preservation after the removal of CTAB and TMB. **c**, Nitrogen adsorption and desorption isotherms of calcined silicages. After CTAB and TMB were removed, particles were calcined at 550 °C for 6 hours in air before nitrogen sorption measurements were taken. A particle synthesis yield of 67% was estimated from the weight of the calcined powder. The surface area of calcined silicages, as assessed by the Brunauer–Emmett–Teller (BET) method, was 570 $m^2 g^{-1}$, consistent with theoretical estimations (Methods). Scale bars in the insets in **b** represent 5 nm.

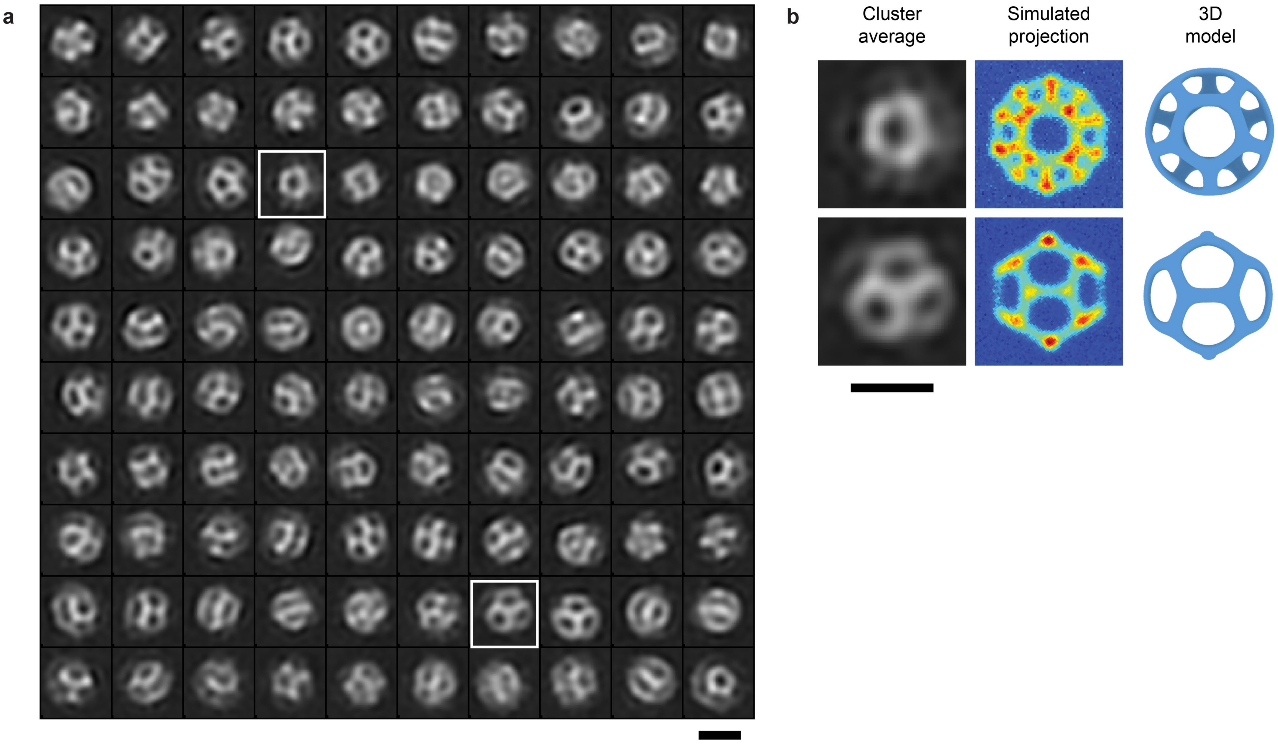

Extended Data Fig. 2 | Cluster averages of two-dimensional images of silicages. **a**, Around 19,000 single-particle cryo-EM images were sorted into 100 clusters[20]. **b**, Some of the projections (examples highlighted in **a**) exhibited features similar to those of simulated projections of dodecahedral cage structure. Also shown are projection models. Scale bars represent 10 nm.

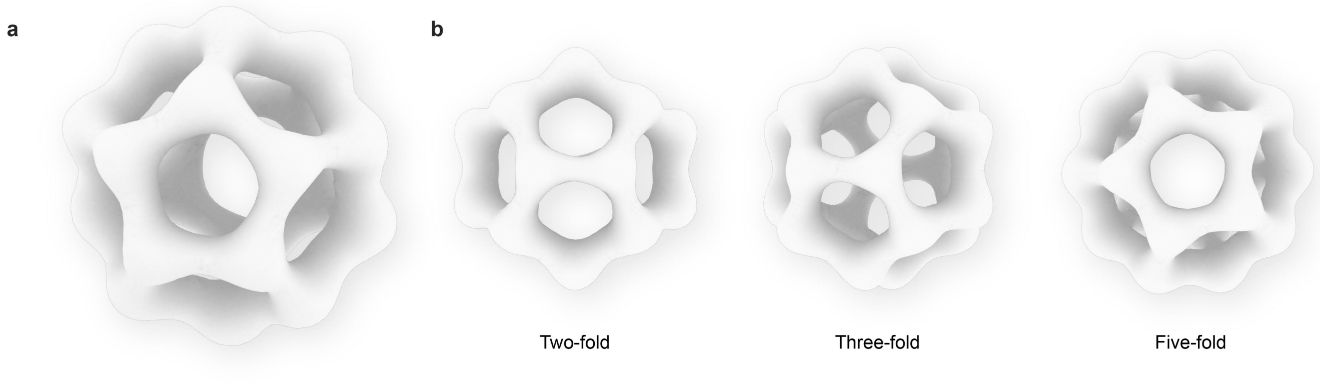

Extended Data Fig. 3 | Reconstruction of a silicage using the RELION 2.1 system. a, Reconstructed dodecahedral silicage[24]. **b**, Its three most unique projections, along the two-fold, three-fold and five-fold symmetry axes. The reconstruction was obtained from a single-class calculation run by RELION 2.1, using the same set of single-particle images as for the dodecahedral cage in Fig. 3a. Visualization is by UCSF Chimera[23].

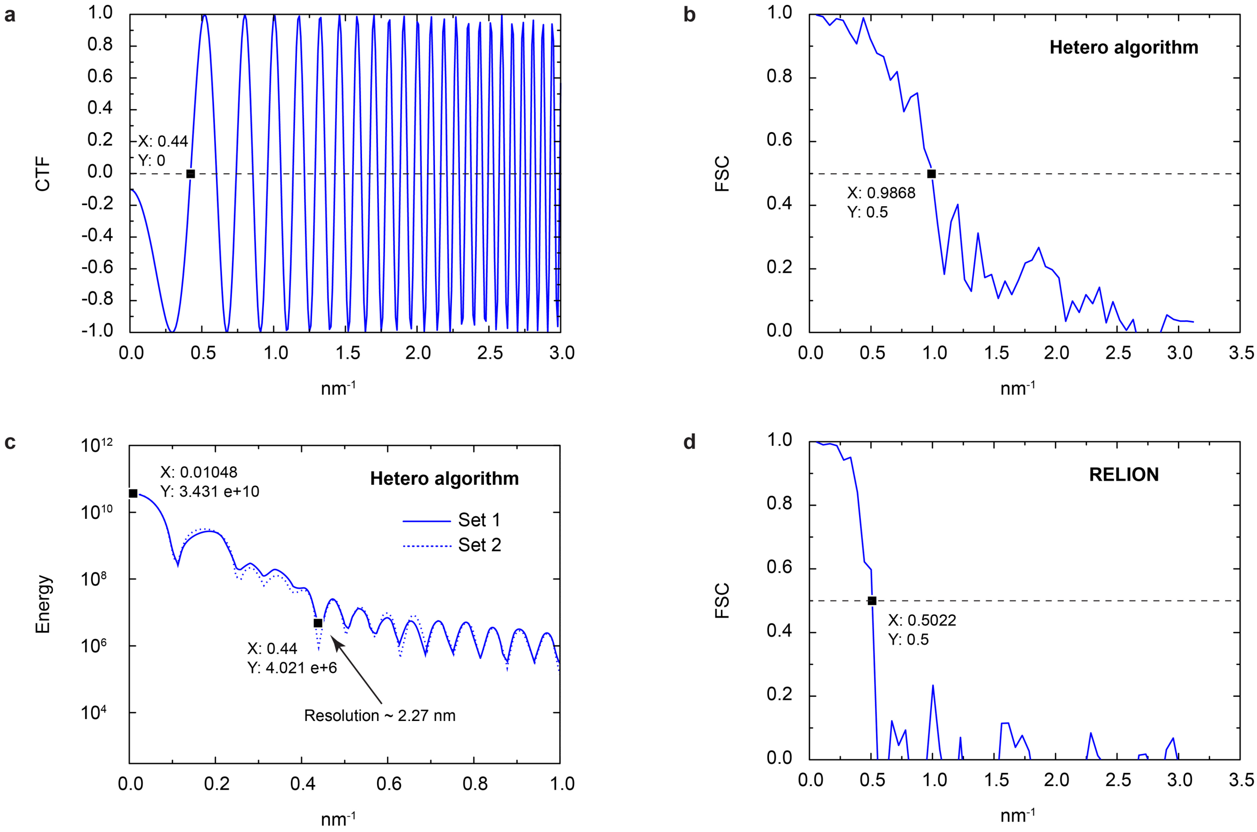

Extended Data Fig. 4 | A typical contrast transfer function, and determination of reconstruction resolution. We used CTFFIND4.1.8 (ref. [25]) to estimate defocus for individual micrographs or a set of micrographs, with results consistent with nominal defocus values of 1–2 μm. **a**, Contrast transfer function (CTF) for a defocus of 1.98 μm. Given that the first zero-crossing of the CTF occurs at 0.44 nm^{-1}, the CTF has little effect on reconstructions unless the resolution is greater than 1/(0.44 nm^{-1}), that is 2.27 nm. **b**, A Fourier shell correlation (FSC)[25] computed by a standard package[20] for two Hetero reconstructions that are independent, starting at the level of separate sets of images each containing 2,000 images (that is, 'gold standard' FSC). The resolution implied by the FSC curve (the inverse of the value of spatial frequency where the FSC curve first crosses 0.5) is 1/(0.99 nm^{-1}), that is 1.01 nm. **c**, Energy function for the same pair of reconstructions as in panel **b**. The energy is the spherical average of the squared magnitude of the reciprocal-space electron-scattering intensity, where the denominator of FSC is the square root of a product of two energy functions, one for each reconstruction. The observation that energy has dropped by more than 10^{-3} times its peak value, and that the character of the curve has become oscillatory and more slowly decreasing—both by 0.44 nm^{-1}—indicates that the resolution implied by the FSC curve is exaggerated[22] and that a more conservative resolution is 1/(0.44 nm^{-1}), that is 2.27 nm. **d**, FSC computed by a standard package[20] for two RELION 2.1 reconstructions computed from the same images as those in panel **b**, from which the resolution (at 0.5 threshold) is estimated to be around 1/(0.50 nm^{-1}), that is 2.00 nm.

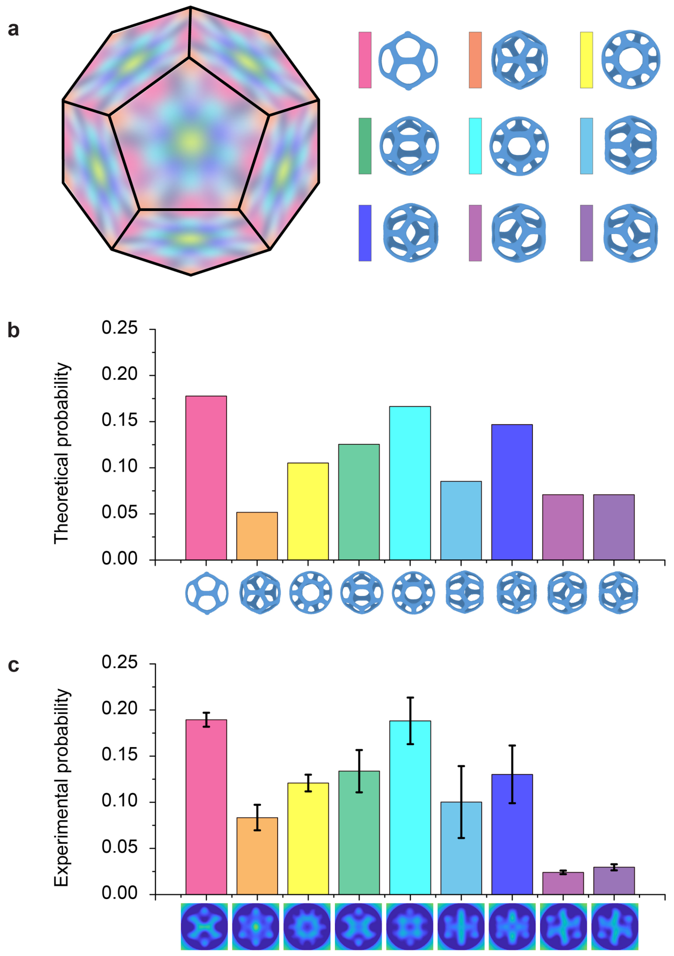

Extended Data Fig. 5 | Probability analysis of silicage projections. **a**, Orientation dependence of silicage projections. Right panel, the nine different silicage projections identified by 3D reconstruction (Fig. 3) are shown. Left panel, these orientations are manually mapped onto the surface of a dodecahedron. The orientations corresponding to different projections are assigned different colours. **b**, Probability analysis for different silicage projections. The probability of imaging a particular projection by electron microscopy is estimated by dividing that subset of the surface area of a sphere that contains the orientations corresponding to a specific projection, by the total surface area of the sphere. **c**, Experimental probability of imaging different silicage projections. The probability of imaging each projection is calculated by dividing the number of single-particle images assigned to a specific silicage projection via 3D reconstruction, by the overall number of silicage single-particle images. The error bars in **c** are standard deviations calculated from three projection distributions, which were obtained from three independent reconstruction runs using different sets of single-particle images.

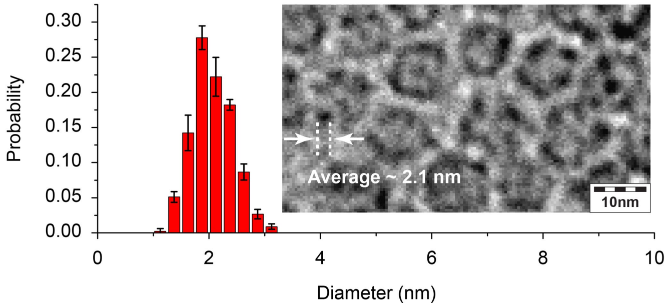

Extended Data Fig. 6 | Size analysis of silica clusters at an early stage of cage formation. Particle-size distribution for primary silica clusters at an early stage of cage formation, obtained by manually analysing 450 silica clusters using a set of TEM images. The measured silica clusters were randomly split into three groups, each containing 150 particles. A cluster-size distribution was then obtained for each of the three groups, and the results were averaged. The error bars are standard deviations calculated from the three cluster-size distributions. A representative TEM image is included at the right. In order to quench the very early stages of cage formation, PEG-silane was added into the synthesis mixture about three minutes after the addition of TMOS, thereby PEGylating early silica structures. TEM sample preparation and characterization were as described in the Methods. Primary silica clusters with diameters of around 2 nm were identified, consistent with the proposed cage-formation mechanism.

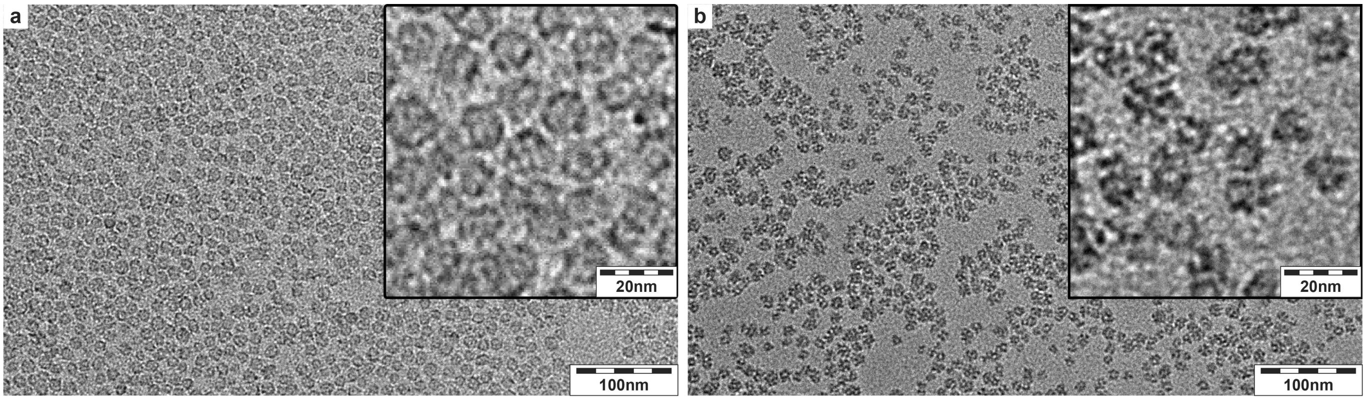

Extended Data Fig. 7 | Role of TMB in cage formation. a, **b**, TEM images, at different magnifications, of silica nanoparticles synthesized with (**a**) and without (**b**) TMB. Nanoparticles synthesized without TMB (**b**) show stronger contrast at the particle centres than do the nanocages (**a**), suggesting that these nanoparticles do not exhibit a hollow cage-like structure but instead are conventional mesoporous silica nanoparticles with relatively small particle sizes.

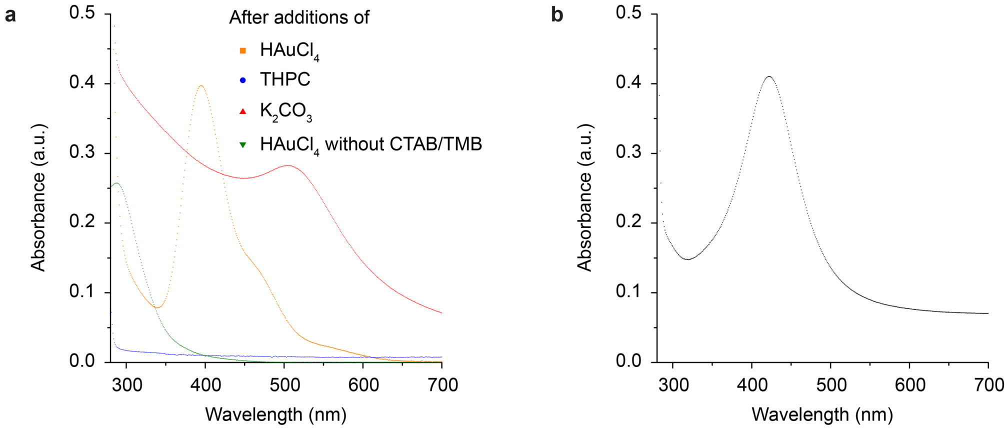

Extended Data Fig. 8 | Optical characterization of gold- and silver-based synthesis solutions. **a**, Survey of the gold-based synthesis, showing the absorption profile of solutions after the successive addition of $HAuCl_4$ (orange) and THPC (blue) and then one day after the addition of K_2CO_3 (red); also shown is the absorption profile when the same concentration of $HAuCl_4$ is added to the equivalent water/ethanol solution but without any CTAB or TMB (green). **b**, Absorption profile of a solution obtained from the silver synthesis 6 hours after the addition of K_2CO_3.

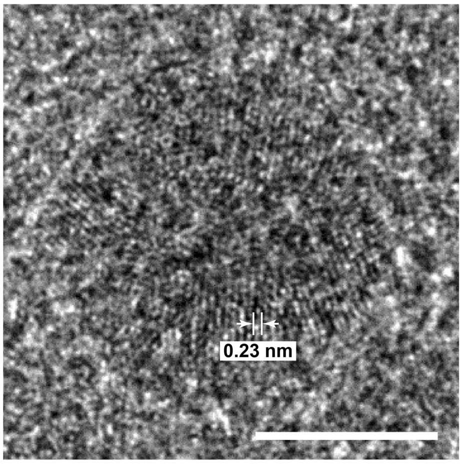

Extended Data Fig. 9 | High-resolution TEM image of a single cage-like gold nanoparticle. This gold particle exhibits lattice fringes with a spacing of 2.3 Å, consistent with the known lattice spacing between (111) planes of gold (Joint Committee on Powder Diffraction Standards no. 04-0784, http://www.icdd.com/). Scale bar represents 5 nm.